PHYSICAL REVIEW A **77**, 033401 (2008)

State-selective imaging of cold atoms

David V. Sheludko,[1] Simon C. Bell,[1] Russell Anderson,[2] Christoph S. Hofmann,[1]
Edgar J. D. Vredenbregt,[3] and Robert E. Scholten[1]
[1]*School of Physics, University of Melbourne, Victoria 3010, Australia*
[2]*Centre for Atom-Optics and Ultra-fast Spectroscopy, Swinburne University of Technology, Hawthorn, VIC 3122, Australia*
[3]*Physics Department, Eindhoven University of Technology, 5600MB Eindhoven, Netherlands*

(Received 3 October 2007; published 5 March 2008)

Atomic coherence phenomena are usually investigated using single beam techniques without spatial resolution. Here we demonstrate state-selective imaging of cold ^{85}Rb atoms in a three-level ladder system, where the atomic refractive index is sensitive to the quantum coherence state of the atoms. We use a phase-sensitive diffraction contrast imaging (DCI) technique which depends on the complex refractive index of the atom cloud. A semiclassical model allows us to analytically calculate the detuning-dependent refractive index of the system. The predicted Autler-Townes splitting and our experimental measurements are in excellent agreement. DCI provided a quantitative image of the distribution of the excited-state fraction, and compared with on-resonance absorption and blue cascade fluorescence techniques, was found to be experimentally simple and robust.

DOI: 10.1103/PhysRevA.77.033401 PACS number(s): 37.10.Jk, 42.50.Ct, 42.30.Wb, 42.30.Rx

I. INTRODUCTION

We have developed an off-resonant imaging technique to investigate atomic coherence phenomena such as electromagnetically induced transparency (EIT) [1], coherent frequency upconversion [2], and “slow light” [3] in a magneto-optical trap (MOT). These processes have typically been studied using techniques without spatial resolution. Imaging offers the potential for obtaining additional information. For example, capture and storage of three-dimensional light fields using EIT [4] could benefit from imaging to provide spatial information about the atomic coherence of the atoms involved. Combining diffraction-based phase imaging with control of the internal state of the imaged atoms using a probe laser, we could potentially explore techniques for enhancing the imaging (e.g., by modifying the refractive index), or for directly measuring the control process itself.

Imaging of the distribution of excited-state atoms has become of interest recently, for example, to control the formation of samples of cold Rydberg atoms [5–7] with defined spatial distribution. Cold Rydberg gas is created by laser cooling and trapping atoms and then exciting them to a Rydberg state, usually in a two-step process which relies on an excitation laser to provide the first excitation step from the ground state (see Fig. 1). The shape of the Rydberg sample can be controlled by spatially profiling the laser beams for either excitation process. Excited-state imaging can provide the feedback to control this process, for example, in dipole blockade [8,9] and coherent excitation [10] experiments.

Imaging feedback is also needed for creating ultracold plasma (UCP) with controlled spatial distribution [11]. UCP is created by photoionization of an ultracold atom cloud, leaving a plasma with very low initial electron (and ion) temperature, which could allow generation of a very-high-brightness electron beam [12]. It has been calculated [13] that the emittance of such a source could be optimized by controlling the initial spatial distribution of the electrons, which is determined by the distribution of excited-state cold atoms and the spatial profile of the photoionization laser. Thus, emittance optimization will require imaging of the excited-state atom distribution, with feedback to the spatial profiles of the excitation and photoionization lasers.

Conventional imaging techniques such as on-resonant absorption imaging are simple and effective. However, absorption imaging is inherently destructive to the cold atom cloud, and critically sensitive to experimental parameters such as defocus, detuning of the imaging laser, and optical alignment. For excited-state imaging, these difficulties are compounded by the need for filters to remove unwanted fluorescence from the image, which introduce noise and interference fringes. Phase imaging techniques, including

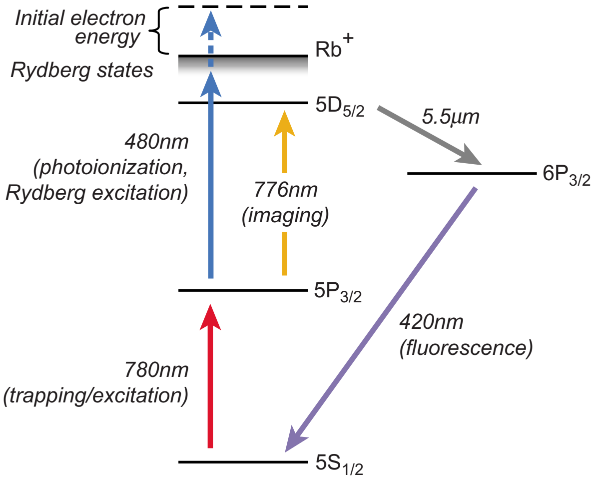

FIG. 1. (Color online) Simplified Rb level scheme showing Rydberg states, ionization threshold, 5*S*-5*P*-5*D* ladder system used for state-selective imaging, and 6*D* state which leads to blue fluorescence at 420 nm. Atoms are cooled and maintained in the excited 5*P* state by the 780 nm laser. A 480 nm beam will excite to Rydberg states or photoionize the atoms, producing cold electrons. The excited-state atom distribution was determined by imaging the 5*P*-5*D* transition at 776 nm.

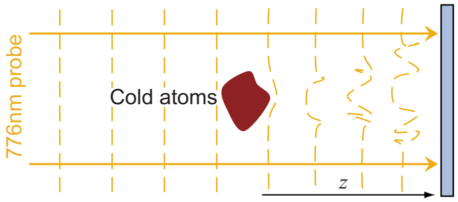

FIG. 2. (Color online) Diffraction contrast imaging records the diffraction pattern of an off-resonant plane wave incident on a cold atom sample.

Zernike phase contrast, are experimentally demanding and quantitative only for a limited range of phase shifts. We have previously demonstrated diffraction contrast imaging (DCI) [14], an off-resonant imaging technique based on retrieving the object phase from Fresnel propagation of a diffracted imaging beam. The technique is quantitative, minimally destructive, and less sensitive to experimental parameters than either conventional absorption imaging or classical phase imaging.

Excited-state imaging is experimentally challenging regardless of the imaging method. The expected incoherent excitation fraction of the $5P$ state is limited to 50% and the natural linewidth of the 776 nm excited-excited transition is only 600 kHz, approximately 10 times smaller than the ground-excited 780 nm transition. The narrow linewidth, and hence slow decay rate from the $5D$ state, limits the absorption of the 776 nm beam. Coupled with the smaller (50%) population in the $5P$ state, it results in low relative absorption (5%) of the 776 nm imaging beam. In combination, the signal-to-noise ratio for simple 776 nm absorption imaging is expected to be 20 times lower than for 780 nm. Fortunately, high atomic density and small cloud size, which are inherently desirable for many applications of interest including UCP production and EIT imaging, enhance the imaging contrast, particularly for diffractive imaging (DCI).

II. THEORY

Figure 2 shows the arrangement for diffraction contrast imaging. An off-resonance probe laser beam incident on a cloud of cold atoms experiences a spatially dependent absorption and phase shift, and then propagates to a spatially resolving detector, such as a CCD camera, which records the object diffraction pattern. Algebraic linear inversion of the Fresnel diffraction relation in Fourier space returns a quantitative measurement of the column density $\mathfrak{p}(\mathbf{x})$ of the sample for transverse spatial coordinates $\mathbf{x} \equiv (x,y)$. The column density of the object is defined as the integral of the atomic number density, $N(r)$ along the optical path:

$$\mathfrak{p}(\mathbf{x}) = \int_{-\infty}^{0} N(r)dz. \tag{1}$$

The relation between the Fourier transform of the normalized contrast of the diffraction pattern, $\mathcal{F}\{(I-I_0)/I_0\}$, and the Fourier transform of the column density at the object, $\mathcal{F}\{\mathfrak{p}(\mathbf{x})\}$, is given by [14]

$$\mathcal{F}\left\{\frac{I-I_0}{I_0}\right\} = 2k[\delta\sin(\pi\lambda z\mathbf{u}^2) - \beta\cos(\pi\lambda z\mathbf{u}^2)]\mathcal{F}\{\mathfrak{p}(\mathbf{x})\}, \tag{2}$$

where $k=2\pi/\lambda$, λ is the wavelength of the probe laser, z is the propagation distance, and $\mathbf{u}$ is the spatial frequency conjugate to $\mathbf{x}$. δ and β are the phase and absorption coefficients, where $\phi=k\delta\mathfrak{p}$ and $\mu=k\beta\mathfrak{p}$ are the phase shift and absorption of the atomic cloud. The refractive index of the atom cloud is then

$$n(\mathbf{x}) = 1 + \mathfrak{p}(\mathbf{x})\frac{\sigma_0\lambda}{4\pi}(\delta + i\beta). \tag{3}$$

The cross section for the imaging transition, σ_0, is defined in terms of the total electron angular momentum quantum numbers J and J' of the ground and excited states of the transition [15],

$$\sigma_0 = \frac{(2J'+1)}{(2J+1)}\frac{\lambda^2}{2\pi}, \tag{4}$$

where we sum all allowed hyperfine levels and magnetic substates for any given probe polarization. Quantitative retrieval of the column density requires knowledge of the (absorption)/(phase) ratio, β/δ, for all transverse position coordinates. Previous work [14] has assumed a two-level atom approximation to derive an analytic (absorption)/(phase) ratio depending only on the probe detuning. For excited-state imaging, a two-level approximation is not appropriate due to the perturbing effect of the excitation laser field. Rubidium atoms in the $5P$ state decay to the ground state via spontaneous emission with a lifetime of approximately 26 ns, much shorter than typical imaging exposure durations (10–100 μs). To maintain atoms in the $5P$ excited state, the 780 nm cooling or excitation light must remain on, perturbing the atomic eigenstates.

A. Complex refractive index

Treating the atom-field interaction semiclassically, the refractive index can be determined using a density matrix formalism [16,17]. The density matrix elements were calculated using optical Bloch equations [18] (OBEs) for three-level atoms ($5S$, $5P$, $5D$; see Fig. 1) with two coupling laser fields. The system is described by six coupled differential equations, which can be solved by numerical integration for steady-state conditions, but an analytical expression for the density matrix elements was achieved by recasting the optical Bloch equations into vector form [19],

$$\frac{\partial\vec{\rho}}{\partial t} = \mathbf{M}\cdot\vec{\rho}, \tag{5}$$

where $\mathbf{M}$ is a 9×9 matrix for a three-level system. Since we want the steady-state solution, the left-hand side of Eq. (5) is $\vec{0}$. Finding the steady-state solution amounts to finding the null space of the matrix $\mathbf{M}$, simplifying the problem considerably. The density matrix elements, and hence the refractive index, are given by the eigenvectors of the system.

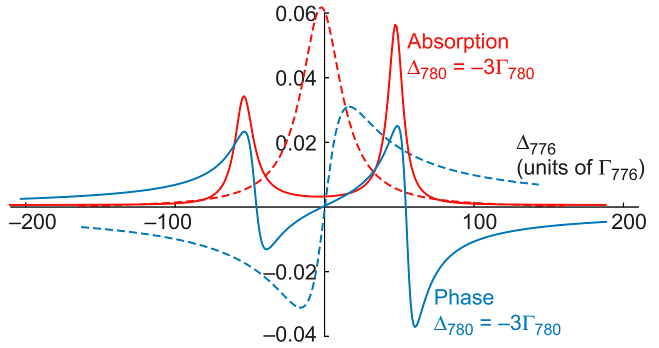

FIG. 3. (Color online) Analytical result for the phase and absorption on the 776 nm transition for a three-level model of Rb, in the weak coupling limit on the 776 nm beam. The two-level results (dashed line) are clearly not valid for excited-state imaging.

The exact solutions for both the real and imaginary parts of the susceptibility were found using this method, each of which contained approximately 100 terms. In the weak coupling limit on the 776 beam, a first-order Taylor expansion gives a more manageable result for the absorption ratio, β/δ,

$$\frac{\beta}{\delta} = \frac{\Gamma_{776}(\Gamma^2 + 4\Delta_{776}^2) + \Gamma\Omega_{780}^2}{2\Delta(\Gamma^2 + 4\Delta_{776}^2) - 2\Delta_{776}\Omega_{780}^2}, \tag{6}$$

where Γ_λ and Δ_λ are the linewidth and detuning of the transitions at wavelength λ, $\Gamma \equiv \Gamma_{780} + \Gamma_{776}$, $\Delta \equiv \Delta_{780} + \Delta_{776}$, and Ω_{780} is the Rabi frequency of the 780 nm laser [20]. The absorption ratio depends entirely on known parameters: Beam detunings, natural linewidths, and the cooling beam Rabi frequency, which can be calculated from the measured excitation beam intensity. The calculated absorption and phase components of the 776 nm susceptibility are shown in Fig. 3, for $\Delta_{780} = -3\Gamma$. Autler-Townes energy level splitting [21,22] is evident in the predicted spectrum of the 776 nm laser, caused by the strong perturbing influence of the applied 780 nm field. The energy level splitting (ΔE) increases with 780 nm detuning and with 780 nm power [23],

$$\Delta E = \hbar\sqrt{\Omega_{780}^2 + \Delta_{780}^2}. \tag{7}$$

To maximize the phase shift and thus imaging contrast, the 776 nm probe must be detuned, e.g., to $+40\Gamma_{776}$. Although not investigated here, imaging as a function of Δ_{776} provides a detailed measurement of the Autler-Townes effect, with spatial resolution. Note that near resonance, the 6 MHz linewidth of the 780 nm transition broadens the effective linewidth of the 776 nm transition. The broadening is reduced by any detuning of the 780 nm excitation beams, so that the expected signal-to-noise ratio (SNR) for excited-state imaging remains low.

A comparison of the first-order approximation [Eq. (6)] with the exact result is shown in Fig. 4, for typical experimental parameters. The energy level splitting shows good agreement. Note that in our image retrieval results we use the exact result for the ratio.

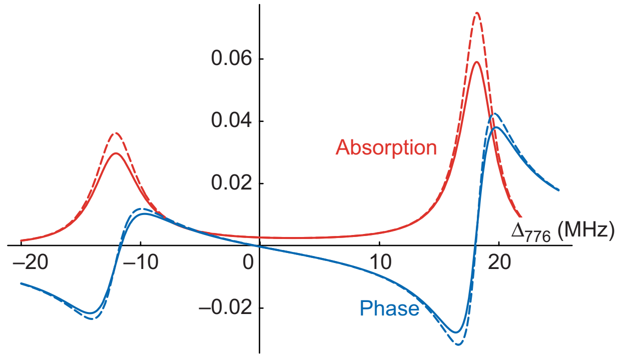

FIG. 4. (Color online) Calculated absorption and phase for the 776 nm transition, showing exact analytic (solid line) and first-order approximation [Eq. (6); dashed line], for typical experimental parameters ($\Delta_{780} = -3\Gamma$, $\Omega_{780} = 30$ MHz).

B. Simulations

The term in square brackets in Eq. (2) is the contrast transfer function (CTF), $h(\mathbf{u}, z)$,

$$h(\mathbf{u}, z) \equiv \delta \sin(\pi\lambda z \mathbf{u}^2) - \beta\cos(\pi\lambda z \mathbf{u}^2). \tag{8}$$

Spatial frequencies corresponding to the zero values in the CTF must be regularized during reconstruction of the column density, to avoid division by zero. This is done by means of the Tikhonov method [24] which smoothly interpolates across the poles. The Tikhonov filtered CTF is given by

$$\frac{1}{h'(\mathbf{u}, z)} = \frac{h(\mathbf{u}, z)}{h(\mathbf{u}, z)^2 + \alpha^2}, \tag{9}$$

where a large value of the Tikhonov parameter, α, increases SNR, but reduces fine detail and increases error in the retrieved column density. A value of $\alpha = 0.1$ to 0.3 is generally acceptable [25].

To determine the accuracy of the retrieval process, a simulation was performed using diffraction patterns calculated from known input column densities. Immediately after the atom cloud, the output wave (at $z = 0$) is described by multiplying the incident wave, f_0, by the complex transmission function of the cloud,

$$f(\mathbf{x}, z = 0) = f_0 \exp[-\mu(\mathbf{x}) + i\phi(\mathbf{x})]. \tag{10}$$

The wave field at an image plane ($z > 0$) is found by Fourier transforming, multiplying by the Kirchoff propagator $\bar{h}(\mathbf{u}, z)$, and inverse Fourier transforming

$$f(\mathbf{x}, z) = \mathcal{F}^{-1}\{\mathcal{F}\{f(\mathbf{x}, z = 0)\}\bar{h}(\mathbf{u}, z)\}. \tag{11}$$

The plane wave free-space propagator is given by

$$\bar{h}(\mathbf{u}, z) = \exp\left(2\pi i z\sqrt{\frac{1}{\lambda^2} - \mathbf{u}^2}\right). \tag{12}$$

The column density was then retrieved from this calculated diffraction pattern using Eq. (2), and compared to the known input column density. A typical diffraction pattern and the retrieved column density is shown in Fig. 5. The incident beam and the atom cloud were constructed and placed asym-

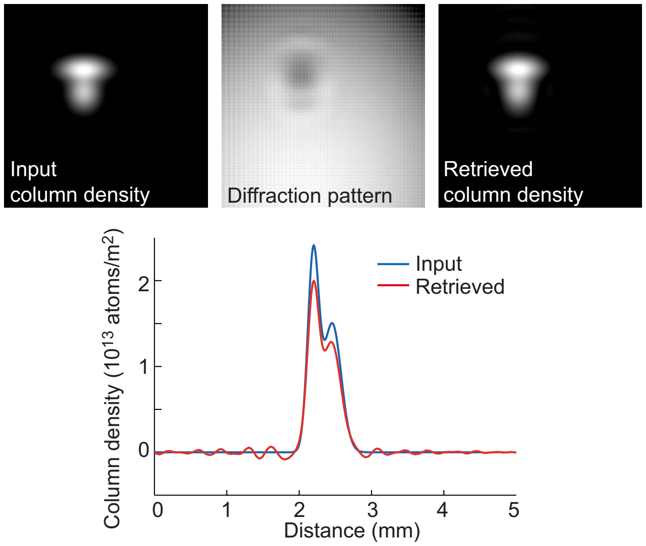

FIG. 5. (Color online) Simulation of diffraction contrast imaging, showing input excited-state column density (left-hand side), calculated excited-state diffraction pattern at $z=130$ mm (center), and retrieved column density (right-hand side). Vertical column density line profiles through the peak are shown below. The 776 nm probe beam was simulated with a Gaussian intensity profile of 5 mm FWHM, detuned 2 Γ_{776} from absorption resonance. The retrieval was regularized with $\alpha=0.2$.

metrically within the image array to ensure that any boundary artifacts of the fast Fourier transform were immediately apparent. The input column density was defined as two overlapping Gaussian column density distributions with different dimensions and peak column densities. The retrieved column density shows good agreement with the initial column density, with noticeable differences introduced only at the peaks of the atom cloud. This error can be reduced significantly by reducing the value of the Tikhonov parameter, α, as shown in Fig. 6, but at the cost of increased high spatial frequency noise. The full width at half-maximum (FWHM) of the retrieved column density profiles remains consistent with the input column density over a much larger range of α values.

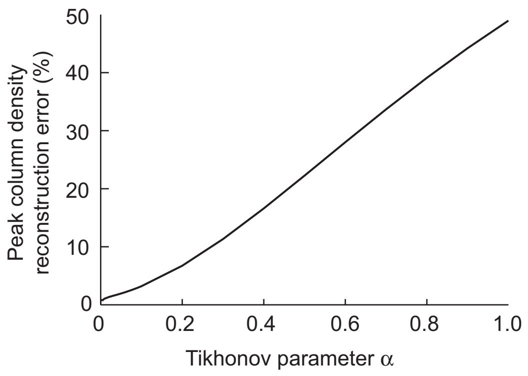

FIG. 6. Normalized error (difference divided by sum) in the peak column density retrieved from simulated excited-state diffraction patterns at a propagation distance of 130 mm, for the object shown in Fig. 5.

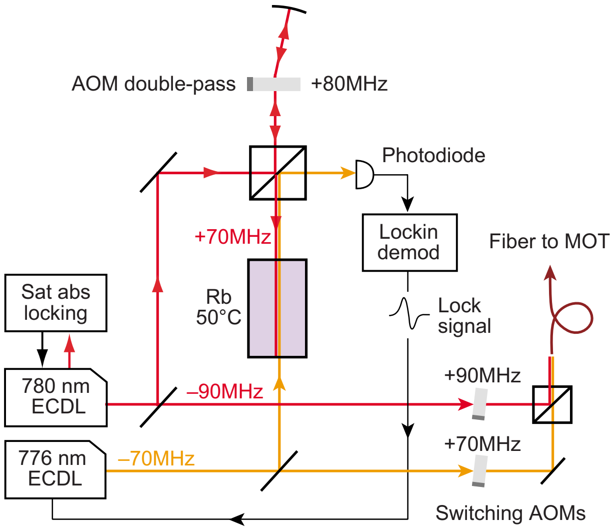

FIG. 7. (Color online) Simplified schematic of the imaging beam locking arrangement. Lenses, mirrors, wave plates omitted for clarity. The frequencies of the laser beams are given relative to the $F=3\rightarrow F'=4$ (780 nm) and $F=4\rightarrow F'=5$ (776 nm) transitions.

III. APPARATUS

Experiments were performed with a magneto-optical trap (MOT) in a $\sigma^{\pm}$ (circularly polarized) arrangement [26,27]. Cooling and trapping were performed on the $5S_{1/2}F=3 \rightarrow 5P_{3/2}F'=4$ hyperfine transition of ^{85}Rb, with external-cavity diode lasers (ECDLs) frequency stabilized using saturated absorption spectroscopy [28–30]. A semiconductor tapered amplifier [31] provided a total cooling beam power of 150 mW at the MOT, after fiber coupling. The cooling beam diameter at the MOT was approximately 20 mm ($1/e^2$). Anti-Helmholtz coils produced a quadrupole magnetic field with a gradient of 10 G/A cm, with a maximum coil current of 6 A. An additional 780 nm repump laser, locked to the $F=2\rightarrow F'=3$ hyperfine transition, was copropagated along one axis of the cooling beams. Rubidium vapor was produced by a dispenser source.

Imaging probe beams at 780 nm and 776 nm were produced with two additional ECDLs. The 780 nm imaging laser was frequency stabilized to the $F=3\rightarrow F'=4$ transition using saturated absorption spectroscopy. The 776 nm imaging laser was frequency-stabilized using Doppler-free two-color spectroscopy (Fig. 7). The 776 nm locking reference beam was counterpropagated through a heated rubidium vapor cell (50 °C), coaxial with a frequency-shifted 780 nm reference produced from the stabilized 780 nm imaging laser via a double-pass acousto-optic modulator (AOM). The AOM frequency was modulated at 250 kHz, and the lock signal generated by demodulation of the dispersive absorption signal of the 776 nm beam. The 776 nm beam could be detuned easily and accurately by varying the 80 MHz AOM carrier frequency. The laser frequencies were offset from their respective resonances to allow for the frequency shift of single-pass AOMs used to provide high-speed switching of the imaging beam. The 776 nm and 780 nm beams were coupled into the same fiber, so that comparable ground- and

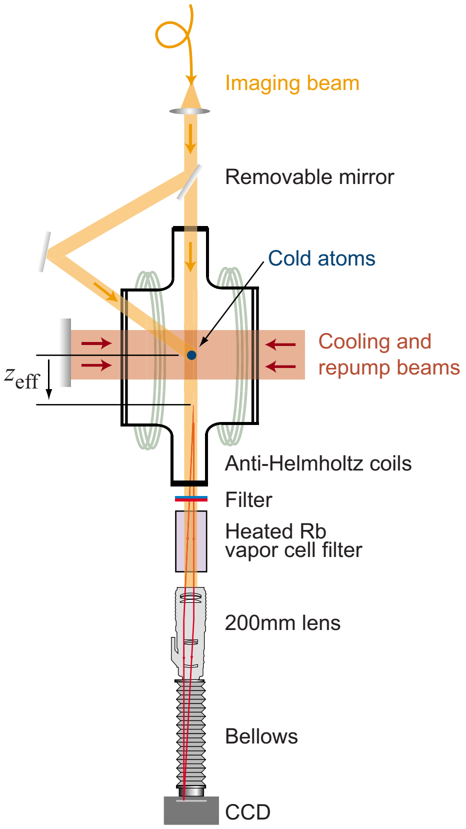

FIG. 8. (Color online) Schematic of the imaging beam path and MOT vacuum chamber. Only two of the six cooling beams are shown.

excited-state images could be acquired consecutively, using either the 776 nm or 780 nm probe beam. Excitation to the $5P$ state was provided by the cooling and trapping lasers, which remained on during imaging.

At the vacuum chamber, the imaging beam from the fiber was collimated to produce a Gaussian beam with $1/e^2$ diameter 10 mm (Fig. 8). A 200 mm lens (micro-Nikkor AF 200 mm $f/4$) allowed the effective defocus distance to be varied, enabling both DCI and in-focus imaging to be performed with minimal changes to the apparatus. Images were taken with a CCD (Apogee Alta U2000 ML 1600×1200 pixels).

Atoms excited to the $5D_{5/2}$ state can decay to the $6P_{3/2}$ state, emitting 5 μm infrared and 420 nm blue light (Fig. 1). The 420 nm fluorescence is proportional to the population in the $5D_{5/2}$ state and thus proportional to the 776 nm absorption. Blue fluorescence images were obtained by directing a 776 nm excitation beam off the imaging axis, to avoid saturating the CCD, via a removable mirror.

780 nm fluorescence created a strong background, substantially reducing the image contrast for 776 nm in-focus absorption imaging, and completely saturating blue fluorescence imaging. To separate the imaging probe beam at 776 nm from the fluorescence at 780 nm, i.e., only 4 nm separation, a very narrow bandpass filter was required. An effective filter was created from a heated rubidium vapor cell. Absorption of the 780 nm fluorescence was much stronger than on the 776 nm probe beam, and a 10 cm vapor cell at 85 °C reduced the 780 nm fluorescence to negligible intensity in a 1 s exposure. The temperature dependence of the 776 nm and 780 nm attenuation is shown in Fig. 9. In addition, a hot or cold filter (Thorlabs FM03, <10% transmission below 630 nm) was used during 776 nm absorption imaging to remove any blue fluorescence. Both filters were removed for 780 nm imaging.

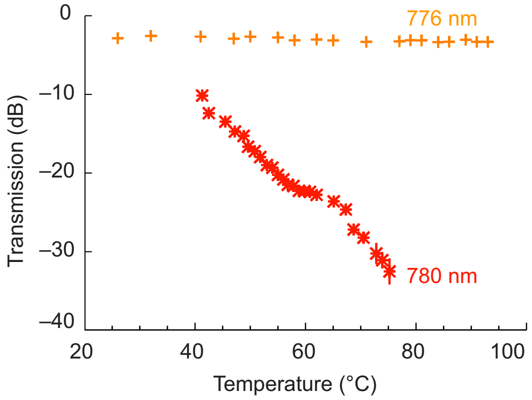

FIG. 9. (Color online) Attenuation of 780 nm and 776 nm light by a heated 10-cm-long vapor cell narrow-bandwidth atomic filter.

Initial 776 nm imaging results exhibited poor signal-to-noise ratio. To increase the atomic density, a compressed MOT (CMOT) technique was employed [32]. Initially, the coils (and hence the trap) were off, to record a background image. The rubidium dispenser was then driven at high current (5 A), the cooling beam detuning set at −6 MHz ($-\Gamma_{780}$) and the coils set at 1 A (10 G/cm) for 30 s to load the trap. The coil current was ramped to a variable maximum (up to 6 A) over times ranging from 5 ms to several seconds. An image was acquired, and the dispenser then returned to a low current (2.5 A) to minimize background gas load, and the coils turned off. The values given are those which optimized the density of the cold atom cloud for our apparatus, limited by a background pressure of 10^{-9} Pa.

It is common to use an additional cooling step with far-detuned light, prior to compression, to increase the atomic density. The additional detuning leads to relatively low excitation and thus was not used in our imaging experiments.

A comparison of 780 nm images taken before and after compression is shown in Fig. 10. Spatial compression of the MOT is clearly apparent, with a peak magnetic field gradient

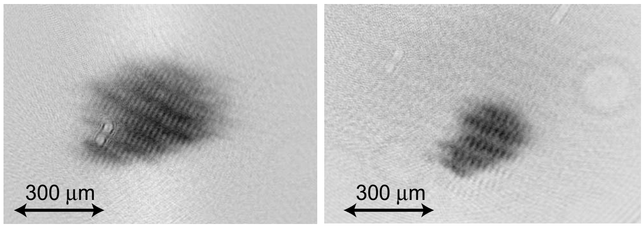

FIG. 10. 780 nm absorption images showing compression due to increase in magnetic field gradient. Uncompressed (left-hand side), field gradient 10 G/cm. Compressed (right-hand side), 100 ms at 50 G/cm. Cloud full width at half-maximum from Gaussian fit, 735 ± 20 μm and 322 ± 12 μm, respectively. Both images: 10 ms exposure, 20 μs pulse duration, 1.5 mW probe beam power.

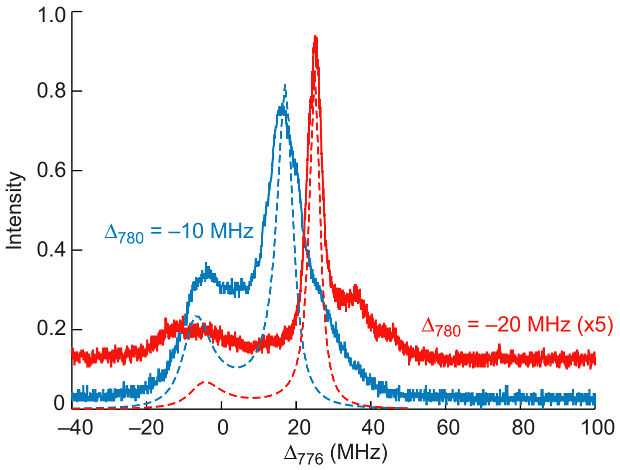

FIG. 11. (Color online) Theoretical (dashed line) and experimental (solid line) 420 nm fluorescence in the MOT for 780 nm cooling beam detunings of -10.0 ± 0.5 and -20 ± 3 MHz.

of 50 G/cm compressing the MOT to approximately one-half the initial diameter, and a peak density up to 4 times higher. The compression was negligible for field gradients below 30 G/cm and also showed only marginal improvement for higher field gradients of 60 G/cm, consistent with findings reported elsewhere [32].

IV. RESULTS

A. Autler-Townes splitting

Our theoretical prediction of Autler-Townes splitting was first tested by measuring the total MOT blue fluorescence, using an integrating detector (not shown in Fig. 8), consisting of a photomultiplier and camera lens (Nikkor AF 50 mm $f/4$) filtered using a 420 ± 10 nm interference filter. The blue fluorescence was recorded as the 776 nm laser was scanned through a frequency range of approximately 180 MHz. The measurement was performed for several 780 nm cooling beam detunings, from -25 MHz to -10 MHz. Example spectra and theoretical predictions are shown in Fig. 11. The dependence on cooling beam power was also verified separately. From Eq. (7) we expect the energy splitting to be less sensitive to cooling beam intensity than detuning, since $\Delta E \propto \Omega_{780} \propto \sqrt{I_{780}}$. This relative insensitivity to beam power explains the close fit of the data, despite the apparent complexity of the system, and also reduces the uncertainty in our imaging results which might arise from fluctuations in cooling beam power. The small shoulder on the right-hand edge of the large peak in the $\Delta_{780}=-20$ MHz spectrum is believed to be due to hyperfine splitting of the $5D$ state. The observed separation of approximately 10 MHz is consistent with the published values of the $5D$ hyperfine splitting [33]. The broadening of the -10 MHz line is due to the larger size of the MOT at this detuning. A larger cloud size results in increased Zeeman detuning across the spatial extent of the atom cloud, broadening the observed fluorescence peaks. The effect is reduced for the much smaller cloud produced by the -20 MHz cooling beam detuning.

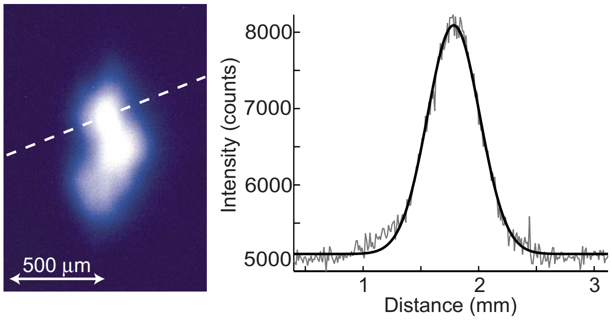

FIG. 12. (Color online) Blue fluorescence image (false color) of the uncompressed MOT for 780 nm excitation and 776 nm probe. 1 s exposure with 21 G/cm magnetic field gradient, 85 °C vapor cell filter temperature. The fluorescence intensity is shown for a profile along the dashed line, with a Gaussian fit.

The cooling beam diameter (20 mm) was much greater than the size of the atom cloud (1 mm). Combined with the relative insensitivity to beam intensity, this minimized any spatial dependence of the refractive index caused by the Gaussian intensity profile of the cooling beams. The excellent agreement for the Autler-Townes splitting provides confidence that our Bloch equation model can reliably calculate the detuning dependence of the refractive index for the 776 nm transition.

B. Blue fluorescence

Blue fluorescence images of the uncompressed MOT were taken using the heated rubidium vapor cell to remove 780 nm fluorescence. The hot or cold filter was removed for these images, and the trapping beams remained on at all times. An example image and line profile are shown in Fig. 12. Due to the long exposure time required, fluorescence images showed considerable blurring, due to the movement of the cold atom cloud on the time scale of the imaging exposure. This lowered the spatial resolution and prevented quantitative imaging.

C. Excited-state absorption

On-resonant in-focus 776 nm absorption images of the compressed cloud were also obtained (Fig. 13). Considerable noise and interference fringes were caused mainly by the many uncoated optical surfaces of the vapor cell and hot or cold filter used in the beam line. The best images were obtained for exposures of 150 μs with probe power approximately 150 μW. From the line profile in Fig. 13, the SNR is ≈ 3, considerably lower than an equivalent ground-state image. This was expected given the relatively low absorption (5%) on the 776 nm beam. Using a Gaussian best fit to the column density line profile, the peak column density calculated from the excited-state absorption image is $(3.1 \pm 0.3) \times 10^{13}$ atoms m^{-2}. The peak column density of the ground-state atom cloud is $(7.0 \pm 0.4) \times 10^{13}$ m^{-2}; thus the excited-state fraction is $44\% \pm 15\%$.

D. Excited-state diffractive contrast

An excited-state diffraction pattern and its column density reconstruction are shown in Fig. 14, together with a ground-

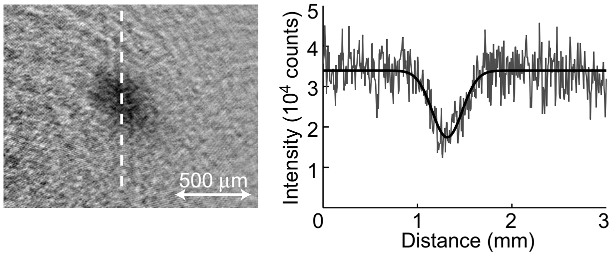

FIG. 13. In-focus absorption image of atoms in the $5P$ state using 776 nm probe beam. Experimental parameters: 60 G/cm peak magnetic field gradient, 4 ms compression, 300 μW probe beam power, 300 μs pulse duration, 1 ms exposure, 85 °C filter cell temperature. Line profile (right-hand side) and Gaussian best fit through the dashed line in the image.

state image for comparison. The excited-state population is $45\% \pm 6\%$, which is in agreement with the absorption image measurement. Using a two-level approximation for our experimental beam powers and detunings, we expect a theoretical excited-state fraction of 46%, in good agreement with our results.

The FWHM of the excited-state cloud, as determined by both DCI and absorption imaging, is much smaller than that of the ground-state cloud (0.42 mm versus 1.18 mm). This difference can be attributed to the combination of the narrow linewidth of the 776 nm transition and the strong magnetic field gradient used to compress the cloud. From Fig. 11, the effective linewidth of the 776 nm transition is approximately 3 MHz for our experimental parameters. The FWHM of the ground-state cloud is 1.18 mm, corresponding to a Zeeman shift of about ± 3 MHz at the half-width at half-maximum of the cloud, for a field gradient of 60 G/cm. The Zeeman shift changes the effective detuning of the probe beam at the outer edges of the cloud, decreasing the absorption and phase shift of the probe light. We anticipate that future work to implement fast switching of the magnetic field coils will provide a direct measurement of this effect.

The DCI reconstructions were less sensitive to noise and interference fringes than in-focus imaging, particularly in the ground-state image. For DCI, the imaging system is inherently defocused from the atom cloud, and so fluorescence (780 nm and 420 nm) will not be in focus. The vapor cell and hot or cold filters were therefore not required, and their interference effects and reflection losses were removed. Results were consistent using defocus distances between 40 and 150 mm and detunings up to 5Γ from the main absorption peak. Due to the narrow linewidth of the 776 nm transition, the reduction in sensitivity to imaging beam detuning compared to absorption imaging makes DCI a robust measurement technique for excited-state imaging.

Excited-state DCI also offers advantages over other techniques for measuring excited-state fraction, including recoil-ion momentum spectroscopy (RIMS) [34], as it does not require additional equipment such as ion beams or RIMS detectors. Our method shows promise for our intended direct application (production of shaped ultracold plasmas) due to its experimental simplicity and minimally destructive interaction. Additionally, by measuring the time evolution of the excited-state fraction and distribution, DCI has the potential to provide valuable information on processes such as stimulated Raman adiabatic passage [35] and allow measurement of the evolution of atomic coherence effects with spatial resolution.

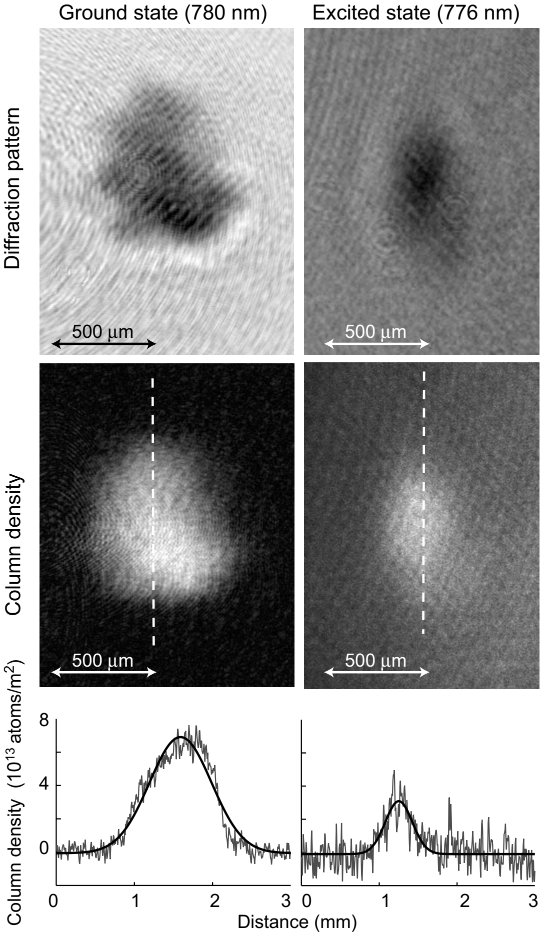

FIG. 14. Ground- and excited-state diffraction patterns, column density reconstructions, and column density line profiles. Experimental parameters for ground-state image: 60 G/cm peak magnetic field gradient, 4 ms field ramp, −6 MHz maximum cooling beam detuning, 850 μW probe beam power, 30 μs pulse duration, 1 ms exposure, $+2.5\Gamma_{780}$ probe detuning, 120 mm effective defocus. For excited-state image: 60 G/cm peak magnetic field gradient, 4 ms field ramp, −6 MHz maximum cooling beam detuning, 150 μW probe beam power, 100 μs pulse duration, 1 ms exposure, +12.5 MHz probe detuning ($+2\Gamma_{776}$ from absorption peak), 130 mm effective defocus.

V. CONCLUSION

Diffraction-contrast imaging offers a simple yet powerful method for imaging cold atom samples, providing spatial information on atomic coherence processes and effects. Quantitative imaging requires knowledge of the ratio of the real to imaginary components of the refractive index of the sample. We have derived an analytic expression for the three-level two-laser system using a semiclassical approach. The model predicts Autler-Townes splitting of the rubidium $5P$ excited state, which was found to be in good agreement with experimental measurements.

We have demonstrated and compared several techniques for state-selective imaging of cold atoms in a MOT. Blue fluorescence imaging provided good SNR, but poor resolution. Excited-state DCI achieved a good SNR without the need for filters, and showed reduced sensitivity to imaging beam imperfections and experimental parameters such as detuning and defocus. The excited-state fraction was found to be $45\% \pm 6\%$, in agreement with theoretical predictions. Conventional (destructive) absorption imaging provided a comparable image, but required a more complicated experimental setup. The need for insertion of filters and a vapor cell in the imaging beamline increases noise and interference fringes in absorption images.

The DCI technique can be adapted to provide spatially resolved measurements of atomic coherence phenomena, such as electromagnetically induced transparency and "slow light," or expanded to investigate more complex multilevel atomic systems. More directly, we will apply the technique for use in feedback control of the spatial distribution of an ultracold plasma, for future application to a high-brightness electron source.

ACKNOWLEDGMENTS

This research was supported by the Australian Research Council Centre of Excellence for Coherent X-ray Science and by the Discovery funding scheme of the Australian Research Council (project ID DP0557505). The work of E.J.D.V. is part of the research program *Stichting voor Fundamenteel Onderzoek der Materie* (FOM), which is financially supported by the *Nederlandse Organisatie voor Wetenschappelijk Onderzoek* (NWO).

---

[1] S. A. Hopkins, E. Usadi, H. X. Chen, and A. Durrant, Opt. Commun. **138**, 185 (1997).
[2] T. Meijer, J. D. White, B. Smeets, M. Jeppesen, and R. E. Scholten, Opt. Lett. **31**, 1002 (2006).
[3] L. V. Hau, S. E. Harris, Z. Dutton, and C. H. Behroozi, Nature (London) **397**, 594 (1999).
[4] M. Shuker, O. Firstenberg, R. Pugatch, A. Ron, and N. Davidson, eprint arXiv:0707.3707.
[5] F. Gallagher, *Rydberg Atoms* (Cambridge University Press, Cambridge, 1994).
[6] S. Bergeson and T. Killian, Phys. World **16**, 37 (2003).
[7] J. Phys. B **38**(2) (2005), special issue on Rydberg physics, edited by R. Côte, T. Pattard, and M. Weidemüller.
[8] M. D. Lukin, M. Fleischhauer, R. Cote, L. M. Duan, D. Jaksch, J. I. Cirac, and P. Zoller, Phys. Rev. Lett. **87**, 037901 (2001).
[9] K. Singer, M. Reetz-Lamour, T. Amthor, L. G. Marcassa, and M. Weidemüller, Phys. Rev. Lett. **93**, 163001 (2004).
[10] J. Deiglmayr, M. Reetz-Lamour, T. Amthor, S. Westermann, A. de Oliveira, and M. Weidemüller, Opt. Commun. **264**, 293 (2006).
[11] T. C. Killian, S. Kulin, S. D. Bergeson, L. A. Orozco, C. Orzel, and S. L. Rolston, Phys. Rev. Lett. **83**, 4776 (1999).
[12] T. Killian, Science **316**, 705 (2007).
[13] B. J. Claessens, S. B. van der Geer, E. J. D. Vredenbregt, and O. J. Luiten, Phys. Rev. Lett. **95**, 164801 (2005).
[14] L. D. Turner, K. F. E. M. Domen, and R. E. Scholten, Phys. Rev. A **72**, 031403(R) (2005).
[15] I. I. Sobelman, *Atomic Spectra and Radiative Transitions* (Springer-Verlag, Berlin, 1979), Vol. 1.
[16] R. Loudon, *The Quantum Theory of Light* (Clarendon, New York, 1973).
[17] M. O. Scully and M. S. Zubairy, *Quantum Optics* (Cambridge University Press, Cambridge, 1997).
[18] L. P. Maguire, R. M. W. van Bijnen, E. Mese, and R. E. Scholten, J. Phys. B **39**, 2709 (2006).
[19] R. M. Whitley and C. R. Stroud, Jr., Phys. Rev. A **14**, 1498 (1976).
[20] D. A. Steck, Los Alamos National Laboratory, available online at http://steck.us/alkalidata
[21] S. H. Autler and C. H. Townes, Phys. Rev. **100**, 703 (1955).
[22] E. W. Streed, A. P. Chikkatur, T. L. Gustavson, M. Boyd, Y. Torii, D. Schneble, G. K. Campbell, D. E. Pritchard, and W. Ketterle, Rev. Sci. Instrum. **77**, 023106 (2006).
[23] C. Cohen-Tannoudji, J. Dupont-Roc, and G. Grynberg, *Atom-Photon Interactions: Basic Processes and Applications* (Wiley, New York, 2004).
[24] A. Tikhonov and V. Arsenin, *Solutions of Ill-posed Problems* (V. H. Winston and Sons, New York, 1977).
[25] L. D. Turner, Ph.D. thesis, University of Melbourne, 2004, http://eprints.unimelb.edu.au/archive/00000822
[26] H. J. Metcalf and P. van der Straten, *Laser Cooling and Trapping* (Springer-Verlag, Berlin, 1999).
[27] C. Wieman, G. Flowers, and S. Gilbert, Am. J. Phys. **63**, 317 (1995).
[28] C. J. Hawthorn, K. P. Weber, and R. E. Scholten, Rev. Sci. Instrum. **72**, 4477 (2001).
[29] L. D. Turner, K. P. Weber, C. J. Hawthorn, and R. E. Scholten, Opt. Commun. **201**, 391 (2002).
[30] MOGlabs laser diode controller, www.moglabs.com
[31] A. C. Wilson, J. C. Sharpe, C. R. McKenzie, P. J. Manson, and D. M. Warrington, Appl. Opt. **37**, 4871 (1998).
[32] W. Petrich, M. H. Anderson, J. R. Ensher, and E. A. Cornell, J. Opt. Soc. Am. B **11**, 1332 (1994).
[33] F. Nez, F. Biraben, R. Felder, and Y. Millerioux, Opt. Commun. **102**, 432 (1993).
[34] X. Flechard, H. Nguyen, R. Bredy, S. R. Lundeen, M. Stauffer, H. A. Camp, C. W. Fehrenbach, and B. D. DePaola, Phys. Rev. Lett. **91**, 243005 (2003).
[35] K. Bergmann, H. Theuer, and B. W. Shore, Rev. Mod. Phys. **70**, 1003 (1998).